A COMPUTATIONAL AND EXPERIMENTAL ANALYSIS OF JOINED-WING AERODYNAMICS

Masakata Hashimoto and Masayuki Ishikawa
Akishima Laboratory, Mitsui Engineering and Ship-Building Co., Ltd.
Akishima, Tokyo, 196 JAPAN
and
Naoki Hirose and Takeshi Ohnuki
National Aerospace Laboratory
Chofu, Tokyo, 182 JAPAN

Abstract

Aerodynamic characteristics of a Joined-wing have been investigated by computational methods and by a low-speed wind-tunnel experiment for the purpose of understanding its aerodynamics characteristics and advantages superior to the conventional configurations and of examining the feasibility of making it fit for a practical application.

The first analysis by the extended-lifting-line-theory and the second analysis by the 3D potential-flow panel method were done to make clear the effects of geometrical parameters on the Joined-wing aerodynamics, such as solid / planar types, span ratio, angles of sweep and area ratio of the front and rear wings. The result showed that the Joined-wing has a wide range of possibility in selecting the geometrical design parameters.

The third analysis by finite difference computation of 3D-Euler equation is applied to obtain the lift and drag characteristics, especially their divergence of the Joined-wing, in the high subsonic to transonic regime. The swept-back front wing was designed to have a wash-out twist distribution and the forward-swept rear wing to have a wash-in distribution and positive incidence in average against the downwash induced by the front wing.

A low-speed wind-tunnel test of 6-component force measurement and flow visualization of the Joined-wing over a wide range of angles of attack up to post-stall gave the lift values which agree well with the computational prediction by the Panel method for the angle of attack up to 8 °. The test showed that the stall characteristics are mild and that the dependence of the lift and drag forces on the side-slip angle is small. Dihedral effect of the front wing and unhedral effect of the rear wing proved to almost cancel out to make the resultant $C_{l\beta}$ very small. Further examinations on effects of the dihedral and unhedral angles and on the location and tail volume of the vertical tail are needed.

Nomenclature

α : Angle of attack — β : side-slip angle
B : Span length — S : Wing area
c : Chord length — Λ : Angle of sweep
Γ : Dihedral / Unhedral angle — λ : Taper ratio
A : Aspect ratio — eA : Effective aspect ratio
C_L : Lift coefficient (=L/qs) — C_D : Drag coefficient (=D/qs)
Cs : side-force coefficient (=Y/qs)
Cm : Pitching moment coefficient (=M/qsc)
Cl : Rolling moment coefficient ($=R/qsB_F$)
Cn : Yawing moment coefficient ($=N/qsB_F$)
Cp : Pressure coefficient — p : Pressure — ρ : Density
u, v, w : Velocity components in x, y, z-direction
Et : Total energy — M : Mach number
q : Dynamic pressure
x , y , z : Cartesian coordinates
ξ , η , ζ : Body-fitted generalized coordinates

superfix

JW : Joined-wing — F : Front wing
R : Rear wing

suffix

∞ : Uniform flow — in : indudced-drag
r : wing root — t : wing tip

I. Introduction

Recent rapid progress in the computational aerodymamics, wide variety of material applications, especially composite materials, and computer-integrated control technology motivates new concepts and designs of unconventional aircraft configurations, some of which have been already under active research and developments.

As one of the unconventional configurations, a concept of three-dimensionally diamond-shaped Joined-wing is proposed. The Joined-wing consists of a swept-back front wing with dihedral angle and a swept-forward rear wing with unhedral angle which is mounted at the top of the vertical tail. The Joined-wing is considered as one of the innovative airplane configurations which is intended to improve flight performance and to achieve the reduction of weight by combining the conventional aft-swept wing and the forward-swept wing.

The following advantages are expected for the Joined-wing;

1) lighter and more rigid,
2) low induced-drag,
3) larger value of maximum lift at trim,
4) low frictional drag by reducing the wetted area, and drag reduction by making the flow laminar with shorter chord length,
5) reduction of wave drag resulting from smooth variation of the sectional area by dividing the wing-body juncture into front and rear portions,
6) innovative control possible by the direct-lift-control (DLC) and the direct-side-force-control (DSC).

Further investigations into the expected advantages superior to the conventional configurations and into issues to be solved in making a Joined-wing fit for a practical application should be made from the point of view of aerodynamics, structural dynamics, controls and engine integration.

Wind-Tunnel test data of the Joined-wing are accumulated and the model airplane is reported to be already flight-tested in the U.S. [1-6] A series of wind-tunnel tests are put in practice also in Japan to understand the fundamental characteristics of the Joined-wing. [7, 8]

In the present paper, the subsonic and transonic aerodynamic characteristics of Joined-wing configurations are reported, by three kinds of theoretical approach, that is, 1) the extended lifting-line theory, 2) the 3D-potential flow Panel methed, 3) a finite difference 3D-Euler analysis, and by a low speed wind-tunnel experiment.

Ⅱ. Theoretical Discussion

Ⅱ-1. Way of approach

In the following theoretical approaches to evaluate the feasibility of the Joined-wing concept, the extended-lifting-line theory is firstly applied for the comparisons between a series of configurations with several geometrical parameters varied.

Then, the potential flow Panel method is applied to investigate the three-dimensional aerodynamic characteristics of the Joined-wing configuration including interaction with a body.

To this step, the optimum configuration which would give full play to the Joined-wing is selected. The third computation to solve 3D-Euler equations by the finite difference method is applied to examine the transonic aerodynamics of an optimum Joined-wing configuration.

Ⅱ-2. Comparative analysis by the extended lifting-line theory

As the first theoretical approach, the extended lifting-line theory[9] taking into account the swept-back angle and dihedral angle of the front wing and the swept-forward angle and unhedral angle of the rear wing of a Joined-wing is formulated to find an answer to the question; what kind of combination of the front and rear wing geometries would provide the higher lift to drag ratio, in other words, the better flight performance. The fundamental equation is given as follows;

$$\alpha(x,y,z) = \sum_{F.R} \frac{1}{4\pi U}\left\{\int_{-B/2}^{0}\Gamma(y')\frac{(x+y\tan\Lambda)}{[(x-|y'|\tan\Lambda)^2+(y-y')^2+(z-|y'|\tan\Gamma)^2]^{3/2}}dy'\right.$$

$$+\int_{0}^{+B/2}\Gamma(y')\frac{(x-y\tan\Lambda)}{[(x-y'\tan\Lambda)^2+(y-y')^2+(z-y'\tan\Gamma)^2]^{3/2}}dy'$$

$$+\int_{-B/2}^{+B/2}\frac{\partial\Gamma}{\partial y}(y')\frac{(y-y')}{[(y-y')^2+(z-|y'|\tan\Gamma)^2]}$$

$$\left.\times\left[1+\frac{x-|y'|\tan\Lambda}{\sqrt{(x-|y'|\tan\Lambda)^2+(y-y')^2+(z-|y'|\tan\Gamma)^2}}\right]dy'\right\} \quad (1)$$

where U is the uniform flow velocity, $\alpha(x,y,z)$ is the angle of attack at the 3/4 C control point, and $\Gamma(y')$ is the strength of the bound vortex of the wing.

Dividing the semi-span of each wing of the Joiend-wing into 10 elements and assuming the unknown strength of vortex $\Gamma(y')$ in each element as constant, the equation (1) is discretized and converted into a simultaneous linear equations, which is solved for $\Gamma(y')$ under the prescribed boundary condition of angle of attack $\alpha(x,y,z)$. The lift and induced-drag forces are computed in terms of $\Gamma(y')$ by the following equations;

$$C_L = \sum_{F.R}\int_{-B/2}^{+B/2}\rho U\Gamma(y')dy'/(\rho U^2 S/2) \quad (2\text{-a})$$

$$C_{Di} = \sum_{F.R}\int_{-B/2}^{+B/2}\rho W(y')\Gamma(y')dy'/(\rho U^2 S/2) \quad (2\text{-b})$$

, where w(y) is the induced velocity at a spanwise station y.

Nine configurations of geometric combination of the front and rear wings composing the Joined-wing which were adopted in the present comparative study are shown in Fig. 1. J3-configuration in the figure is taken as a basic one for the comparison, which has the following specifications of geometry;

	Front wing	Rear wing
Aspect ratio	8	8
Taper ratio	0.5	0.5
Sweep angle	+30° (Aft Swept)	-30° (Forward Swept)
dihedral / unhedral angle	+10° (dihedral)	-10° (unhedral). (without twist distribution)

Comparisons are made between the basic and the other configurations in terms of values of lift and induced drag at $\alpha = 2°, 4°, 6°$.

a) Typical lift and induced-drag distributions

The spanwise lift $C_l(y)$ and induced-drag $Cdi(y)$ distributions at $\alpha = 2°$ of J4 configuration are shown in Fig. 2 and 3 as one of typical examples. The sectional lift at each spanwise station and the resulting total lift of the Joined-wing are less than the simple sum of lifts of the front-wing-alone and the rear-wing-alone, where the lift of rear wing is reduced by downwash effect from the front wing.

Locally in the viscinity of the joint, a noticeable reduction of induced-drag Cdi is observed, that is considered to be resulting from the strong upwash effect induced by the bound vortex and trailing vortex of the rear wing to the front wing.

b) Planar-type (J1) and solid-type (J3) Joined-wings

Lift-to-drag ratios of planely diamond-shaped 'planar-type' Joined-wing (J1) and a three-dimensionally diamond-shaped 'solid-type' Joined-wing (J3) where the front and rear wings have 10° dihedral and 10° unhedral respectively and are separated by 1.06 times the chord length at the wing root are compared. The solid-type joined-wing (J3) shows higher lift-to-drag ratio values as shown in Fig. 4. This is explained by the vertical separation between the front and rear wings of the solid-type Joined-wing, which makes the downwash effect on the rear wing by the front wing relatively small and makes the lift of the rear wing closer to the one of the wing alone.

c) Effect of ratio of rear wing span/front wing span

Span length of the rear wing is varied from 6 of the basic configuration J3 (Aspect ratio A =8) to 4 of J4 (A=5.3), 3 of J5 (A=4), and 2 of J6 (A=2.7), while keeping the front wing span constant equal to 6. The computed results of lift and induced-drag are shown in Fig. 4. The shorter the rear wing span is, the higher the lift-to-drag atio becomes, approaching to the result of the front-wing-alone configuration (J2). The same data are shown in Fig. 5 as a relation of the effective aspect ratio $e \cdot A = C_L^2/\pi \cdot C_D$

to the rear / front wing span ratio B_R/B_F, where the smaller value of the rear wing span B_R corresponds to the larger value of effective aspect ratio, approaching to the one of the front-wing-alone configuration. It is noted that the effective aspect ratio of the each configuration is very close to the value, which is derived by taking the front wing span B_F as a reference span length and the sum of the front and rear wing areas as a reference area.

d) Effect of swept-back angle of the front wing and swept-forward angle of the rear wing

The swept-back angle of the front wing Λ_F and swept-forward angle of the rear wing Λ_R are varied as (Λ_F, Λ_R)=(30 ° ,30 °) of J4, (0 ° , 30 °) of J8, and (30 ° , 0 °) of J9 configurations , keeping the front wing span length equal to 6 and the rear wing span length egual to 4. Lift vs. induced drag characteristics of the three configurations shown in Fig.4 almost coincide, although there exist differences of load allotment on the front and rear wings. For the same value of angle of attack α, the J8 or J9 configuration, in which either of the front or rear wing is rectilinear wing, shows higher values of both lift and induced drag than the J4 configuration, in which both of the wings have angles of sweep.

If J8 and J9 are compared, the J9 configuration, with a swept-back front wing and a rectiliner rear wing, provides higher values of lift and induced drag than J8.

e) Way of Joint

The effect of way of joining the front and rear wings are examined by making a comparison between J4 and J7 configurations keeping the other geometrical dimensions the same. In the former, the leading edge of the rear wing is joined to the trailing-edge of the front wing at the spanwise station of joint , while, in the latter, both leading edges of the front and rear wings are joined together. The polar curves in Fig.4 shows little difference in the lift to induced-drag characteristics, though the values of lift and induced-drag at the same angle of attack are higher in J4 than J7.

II-3. Comparative analysis by Panel method

In order to put forward the configuration comparisons taking into account chordwise load distribution and aerodynamic interaction between a wing and a body, aerodynamic computations for whole aircraft configurations with the front and rear wings and a body are made by the Panel method developed by Morino[10] of a 3D-potential flow. The governing equation is given as follows ;

For the disturbance velocity potential ϕ,

$$\phi_{xx}+\phi_{yy}+\phi_{zz}=0 \qquad (3a)$$

with the boundary conditions,

$$\vec{\ } \quad \vec{\ } \quad \vec{\ }$$

1) $\phi_n = -u \cdot n$ (n : unit normal) (3b)

2) $\Delta\phi=\phi_+-\phi_-$ on the wake vortex sheet (3c)

3) $\phi\infty=0$.

Discretized form for the Panel method : $\rightarrow \quad \rightarrow$

$$[\delta_{hk}-C_{hk}-W_{hk}]\{\phi_k\}=[b_{hk}]\{u\cdot n_k\} \qquad (3e)$$

where δ_{hk} : kronecker's delta

$$C_{hk}=\left[\frac{1}{2\pi}\iint_{\Sigma_K}\frac{\partial}{\partial n}\left(\frac{1}{R}\right)ds\right]_{p=p_h} \qquad (3f)$$

$$W_{hk}=\left[\pm\frac{1}{2\pi}\iint_{\Sigma_K{}'}\frac{\partial}{\partial n}\left(\frac{1}{R}\right)ds\right]_{p=p_h} \qquad (3g)$$

$$b_{hk}=\left[\frac{1}{2\pi}\iint_{\Sigma_K}\frac{1}{R}ds\right]_{p=p_h} \qquad (3h)$$

Lift and induced-drag forces are computed by integrating the pressure distribution.

Seven joined-wing-body configurations are shown in Fig.6. Both front and rear wings have the aspect ratio 8, taper ratio 0.5, uniform incidence 3 ° and the wing section is NACA23012. The cylindrical body smoothly shaped at the nose and the tail is common to all configurations. The vertical tail has the aspect ratio 1 and the wing section is NACA0009. Numbers of panels used are 168 for the body (circumferential 6×streamwise 26 +12), and 100 + 100 for the front and rear wings (chordwise 20× spanwise 5) resulting in 368 in total.

a) Comparison between a Joined-wing and the front- or rear-wing-alone configurations

Aerodynamic interaction effect between the front and rear wings' is examined by making comparison between the Joined-wing (JW1), the front-wing alone (JW2) and the rear-wing alone (JW3) configurations. The front wing has a swept-back angle of 34.8° ,dihedral of 12.7 ° ,and the rear wing has a swept-forward angle of -27.0 ° and unhedral of -24.9 ° .

Pressure distributions over the wings are shown in Fig.7. Spanwise lift and induced-drag distributions are shown in Fig.8 as for JW1 and in Fig.9 as for JW2 and JW3. As a result of joining two wings, the lift becomes less and the induced-drag becomes greater in JW1 than the simple sums of the ones of JW2 and JW3.

As for the front or rear wing respectively, 1) the lift changes little in the front wing, while it is reduced in the rear wing by the downwash effect induced by the front wing and 2) the induced-drag increases in the front wing on the whole , while it shows little change in the rear wing.

b) Area ratio between the front and rear wings

Wing area ratio of the front and rear wings S_F/S_R is varied as,

S_F / S_R = 1 / 1 (JW1)
= 3 / 1 (JW4)
= 1 / 3 (JW5)

, while the total wing area $S = S_F + S_R$ is kept constant. Lift and induced-drag vs. S_R/S relations of the three configurations are plotted in Fig.10. The lift load allotment to the front and rear wings, that is the pitching moment, changes with S_F/S_R variation. The total lift is greater and the induced-drag is less in JW5(S_R/S =0.67), than JW4 (S_R/S =0.33). The relatively large front wing in JW4 causes the lift of the rear wing reduced by its downwash effect. The induced drag is the largest in JW1 (S_R/S =0.5) among the three configurations.

c) Effect of swept-back angle of the front wing

The swept-back angle of the front wing and the swept-forward angle of the rear wing are varied as,

(Λ_F , Λ_R) = (34.8 °,-27.0 °) (JW1)
= (-2.7 °,-51.3 °) (JW6)

$= (49.2\ ^\circ, -2.7\ ^\circ)$ (JW7)

where the total wing area is kept constant and the wing area ratio is 1. The total lift to induced-drag relation of the three configurations hardly differ due to the angle of sweep as shown in Fig.11. This is regarded as a consequence of cancellation of the swept-back and swept-forward effects of the front and rear wings. Daring to cite any difference, both values of lift and induced-drag are small in JW6 where both of the front and rear wings are swept forward, or in JW7 where the swept-back angle of the front wing is large.

Ⅱ-4 Transonic analysis by a 3D-Euler code

A finite difference method to solve 3D-Euler equations is applied to analyze the aerodynamic characteristics of a Joined-wing configuration.[11]

The governing equations are a non-dimensionalized system of Euler equations composed of continuity, momentum and energy equations, and an equation of state in the 3D body-fitted generalized coordinates (ξ, η, ζ).

$$\frac{\partial \hat{U}}{\partial t} + \frac{\partial \hat{E}}{\partial \xi} + \frac{\partial \hat{F}}{\partial \eta} + \frac{\partial \hat{G}}{\partial \zeta} = 0 \qquad (4)$$

where

$$\hat{U} = | \rho,\ \rho u,\ \rho v,\ \rho w,\ E_t | / J \qquad (5)$$

The independent variables are density ρ, momentums ρu, ρv, ρw and total energy E_t. J, ξ_x's are Jacobian and metrics of the coordinate transformation. The equation of state of perfect gas is used together.

The boundary conditions are imposed in the following manner :

1) Uniform flow values are assumed at far upstream and far side boundaries.
2) Tangential slip surface condition is applied on the wing surface.
3) Linear extrapolations are used except pressure assumed equal to the uniform flow value.
4) Linear extrapolations are used with W=0 also at symmetry plane boundary of the wing center line.
5) Linear interpolations from upper and lower halves of flow field are used for wake surfaces.

The time-split, two-step, second-order MacCormack's scheme [12] is applied to the time-dependent conservation form of eq. (4) by using finite difference grid (j,k,l) stretched over the generalized coordinate (ξ, η, ζ). The grid is C-type around a wing chordwise section and H-type in the spanwise direction. One of the grid systems used for the computations is shown in Fig.12.

The operation from time step 'n' to step 'n+1' is given as follows :

$$\hat{U}^{n+1}_{jkl} = L_{\xi\eta\zeta}(\Delta t) \cdot \hat{U}^{n}_{jkl} \qquad (6\text{-a})$$

where

$$L_{\xi\eta\zeta}(\Delta t) = L_{\xi}(\Delta t/2) \cdot L_{\eta}(\Delta t/2) \cdot L_{\zeta}(\Delta t/2) \cdot L_{\zeta}(\Delta t/2) \cdot L_{\eta}(\Delta t/2) \cdot L_{\xi}(\Delta t/2) \qquad (6\text{-b})$$

The Jameson-type 3rd-order, 4th-derivative and 1st-order, 2nd-derivative artificial viscosity terms[13] were added for the numerical stability and for obtaining a sharp shock wave.

The Joined-wing model adopted has the following configuration shown in Table 1 ; The front wing has the aspect ratio 8.0, the taper ratio 0.31 , the swept-back angle 30 ° and the dihedral angle 10 °. The rear wing has the aspect ratio 4.76, the taper ratio 0.31, the swept-forward angle 30 ° and the unhedral angle 20 °.
The spanwise twist angle distributions were determined after a series of iterative computations to make both of the front and rear wings carry almost elliptic lift load distributions even in the upwash / downwash interaction flow field between the two wings. The front wing, then, has the twist destribution linearly varying from -1 ° at the root to +1 ° at the tip. The rear wing has the twist distribution linearly varying from -1 ° at the root to -3 ° at the tip.

Mach number is varied over the range of $0.5 \leqq M\infty \leqq 0.95$, and the angle of attack is set in the range of $0\ ^\circ \leqq \alpha \leqq 6\ ^\circ$ which contains $\alpha = 4\ ^\circ$ corresponding to the design C_L .

a) Lift characteristics

Lift coefficient C_L vs. angle of attack α characteristics at the design Mach number $M\infty = 0.75$ are shown in Fig.13 . The lift curve of the Joined-wing is almost linear over the angle of attack range around $\alpha = 4\ ^\circ$ for design lift coefficient $C_L = 0.4$, where $C_L^F / C_L^R = 0.474 / 0.275$ and the allotment of lift load is $L^F / L^R = 2.87$.

Lift coefficient C_L vs. drag coefficient C_D at $M\infty = 0.75$ is shown in Fig.14. The airplane efficiency, that is the effective aspect ratio defined by $eA = C_L^2/\pi C_D$ of the present configuration is higher than the configuration without incidence distribution for the lift coefficient range $C_L > 0.3$ that contains $(C_L)_{design} = 0.4$.

Lift coefficient C_L vs. Mach number $M\infty$ characteristics at $\alpha = 4^\circ$ are shown in Fig.15. Although the rear wing is designed to have +2 ° more incidence than the front wing in average taking into account the downwash effect, the lift coefficient of the front wing C_L^F is still higher than the one of the rear wing C_L^R in this condition of $\alpha = 4^\circ$. The lift coefficient of the Joined-wing C_L^{JW} comes between the values of C_L^F and C_L^R, that is, $C_L^F > C_L^{JW} > C_L^R$.

The lift coefficients of the front wing C_L^F and of the Joined-wing C_L^{JW} show the lift divergence characteristics; that is, they have the maximum values at $M\infty = 0.9$ and decrease above it, while the variation of C_L^R of the rear wing is small. The lift load allotment on the front wing is relatively so large that the whole lift characteristics of the Joined-wing are mainly determined by the one of the front wing.

The section lift coefficient distribution C_l shown in Fig.16 is larger at the outer spanwise region than the inner one of the front wing, though the spanwise load

$C \cdot C_l$ is designed to have an elliptic distribution; actually the lift coefficient C_l of the front wing reaches to 0.70 at the 90% spanwise station when M_∞=0.85. The high value of C_l in the tip region of the front wing governs the lift divergence characteristics of the whole Joined-wing.

b) Drag characteristics

The drag coefficient C_D vs. Mach number M_∞ characteristics are shown in Fig.17. As the present computation is based on the Euler equation, the drag is the sum of the induced-drag and wave drag. $C_D{}^{JW}$ and $C_D{}^F$ remain almost constant up to M_∞ =0.70, but those increase rapidly for $M_\infty \geqq 0.75$. Drag divergence Mach number M_{DD} defined by $\partial C_D / \partial M_\infty = 0.1$ is $(M_{DD})^F = 0.77$ for the front wing and $(M_{DD})^{JW} = 0.78$ for the whole Joined-wing. Drag coefficient of the rear wing is less than the one of the front-wing-alone or the Joined-wing, that is, $C_D{}^F \geqq C_D{}^{JW} > C_D{}^R$.

The drag characteristics of the whole Joined-wing are principally determined by the front wing. Consequently, the drag divergence of the whole Joined-wing depends mainly on the one of the front wing, especially on the rapid development of shock wave strength in the front wing tip region.

c) Pressure distribution

Cp-contours over the upper surfaces of the Joined-wing for M_∞=0.65, 0.75 and 0.85 with α=4° are shown in Figs.18(a) (b) (c). The corresponding chordwise pressure distributions C_P vs. x/c at four spanwise stations are shown in Figs.19(a) (b) (c).

When M_∞=0.65, the leading-edge suction peak grows up in the region of the front wing outer than its 30% spanwise station and C_P becomes slightly greater than the critical value $C_P{}^*$ at 80% spanwise station, though no shock wave is observed. The rear wing has larger L.E. suction peak in the inner wing region, which is the general characteristics of the forward-swept wing. But there is no shock wave even at 6% spanwise station.

When M_∞=0.75, the leading-edge suction peak of the front wing becomes larger than that of M_∞=0.65, which results in the existance of the shock wave in the region outer than 50% spanwise station. The L.E. suction peak in the inner wing region of the rear wing increases, but no shock wave is observed yet.

As a whole for M_∞=0.65 and 0.75, the isobar lines are almost straight in the wing spanwise direction, except some distortion observed around the joint.

When M_∞=0.85, the shock wave exists at 60 ～80% chordwise location along the entire span of the front wing, while it exists at 30 ～40% chordwise location along entire span of the rear wing. The isobar lines do not lie straight in the wing spanwise direction any longer at this condition of M_∞=0.85 and α=4 ° actually in the midst of lift and drag divergences.

Ⅲ. Low-Speed Wind Tunnel Test

A series of low-speed wind tunnel tests of a Joined-wing were done to collect the data of its lift, drag and side forces and of its pitching, rolling and yawing moments over the wide range of angle of attack α with the angle of side-slip β as a parameter. The wind-tunnel model of a diamond-shaped Joined-wing used in the present experiment is shown in Fig.20 and Fig.21. The dimensions of the model are the same as those used in the 3D-Euler analyses in Ⅱ-4, but it does not have any spanwise twist distribution. The tip leading-edges of the rear wing are connected to the trailing edges of 60% semi-span of the front wing with no overlap. The cylindrical body smoothly shaped like a cone at the nose and tail has a length of 1m and a diameter of 0.1m.

A 6-component force measurement and a flow visualiztion by oil-flow technique were made for the following three configuratoins ;

1) Joined-wing configuration,
2) Front-wing configuration,
   (Front wing+Vertical tail+Body)
3) Rear-wing configuration,
   (Rear wing+Vertical tail+Body)

The wind velocity is kept constant at 20m/sec which yields the Reynolds number $Re = 1.5 \times 10^5$ based on the front wing root chord length. The angle of attack α is set in every 2 ° between 0 ° and 14 ° and in every 1 ° between 15 ° and 20 ° . The side-slip angle β is set at 0 ° ,3 °,6 °and 9 ° . The measured force and moment values were non-dimensionalized with the mean chord length of 0.115m and the span length of the front wing of 0.84m. The reference point of the moment is selected at the point 0.45m downstream from the nose of the body.

a) Lift characteristics C_L

For the range of angle of attack α= 0 ° ～ 8 ° in all of the three configurations, the lift coefficient C_L varies linearly with α, and coincides well with the computationally predicted values by the Panel method. For the angle of attack α>8 ° ,the lift curve slope $C_{L\alpha}$ decreases gradually, due to flow separation spreading over the front wing upper surface. This was confirmed by the oil-flow visualization. The stall characteristics are mild in all cases.

The effect of side-slip angle β was investisated. Little difference in the lift characteristics among the three configurations is found for α= 0 ° ～12 ° . However, the larger value of β corresponds the more lift coefficient C_L for the angle of attack α= 14 ° ～ 20 ° of the Joined-wing (Fig.22) and the front-wing alone configurations. And the larger the β is, the higher the stall angle of attack is. Phenomenologically, what the lift still increases, for example, at α= 20 ° and β=9 °, is interpreted by the oil-flow visualization as the additional lift due to separation vortices shedding from the wing-body junctures. On the other hand, in the rear-wing alone configuration, the larger β corresponds to the smaller value of the lift coefficient for α= 14 ° ～20 ° .

b) Drag characteristics C_D

The drag coefficient remains constant up to α=8 ° for the Joined-wing and the front-wing configuration, or up to α= 14 ° for the rear-wing configuration. It shows rapid increase due to the flow separation spreading over the front wing upper surface when the angle of attack α is greater than the above-mentioned values (Fig.23).

The effect of side-slip angle β on the drag coefficient value is negligible. But, it is remarked that the larger β produces the smaller drag for the angle of attack ranging α=14 ° ～20 ° in the rear-wing configuration. This is because, in the rear wing configuration, the larger β produces the smaller lift which results in the smaller induced-drag values.

c) Side-force characteristics C_s

The side force produced is negative as a restoring force against the side-slip in the three configurtions, the absolute value of which is greater for the larger angle of side-slip angle β.

In the Joined-wing(Fig.24) and the front-wing configurations, the absolute value of the side force $|C_s|$ decreases with α for $\alpha > 8°$ when the flow separation occurs. For example, the value $|C_s|$ at $\alpha = 20°$ is almost 50% of the value at $\alpha = 10°$.

On the other hand, in the rear-wing configuration, the absolute value of the side force $|C_s|$ increases for $\alpha = 12° \sim 16°$, then decreases for $\alpha = 12° \sim 16°$. These characteristics of $|C_s|$ are supposed to depend on the complex phenomenon that the side flow coming into the vertical tail and the body changes with α and β.

d) Pitching moment characteristics C_m

The pitching moment produced is negative in the three configurations, the absolute value of which $|C_m|$ increases with α.

The variation with α is not linear; for example, in the front-wing configuration, $|C_m|$ remains almost constant up to $\alpha = 8°$, then increases.

$|C_m|$ differs little with the side-slip angle β in the Joined-wing(Fig.25) and the front-wing configuration, while the lager β produces the smaller value of $|C_m|$ for $\alpha \geqq 10°$ in the rear-wing configuration. This is explained by the afore-mentioned small lift values at this condition.

e) Rolling moment characteristics C_l

The rolling moment C_l is positive for the side-slip angle $\beta = 0°$ and $3°$ in the Joined-wing and the front-wing configurations, and for all values of β tested in the rear-wing configurations.

The derivative of the rolling moment C_l with β, $C_l\beta$, is positive for $\beta = 0° \sim 3°$ and negative for $\beta = 3° \sim 9°$ in all of the three configurations.

In general, $C_l\beta < 0$ is required from the design standpoint for the airplane stability. The rolling moment of a Joined-wing is principally determined by the lift difference between the right and left wings and by the side force and its point of action ;the rolling moment becomes negative $C_l < 0$ (left wing downward) by the swept-back angle and the dihedral angle of the front wing and by vertical tail, while it becomes positive $C_l > 0$ (right wing downward) by the swept-forward angle and the unhedral angle of the rear wing and by the body.

The rather complicated characteristics of the rolling moment obtained in the present wind-tunnel experiment can be explained by the following reasons; 1) the height of the vertical tail is too small in the front-wing configuration. 2) In the rear-wing alone configuration, the unhedral is too large and the vertical tail is covered from the side-wash by the rear wing. 3) For the small value range of β in the Joined-wing configurations, the dihedral effect $C_l\beta < 0$ of the front wing is cancelled out by the value $C_l\beta > 0$ of the rear wing, and the height of the vertical tail is insufficient, 4) When the side-slip angle β is large, the side force produced at the verical tail becomes large enough for $C_l\beta < 0$.

f) Yawing moment characteristics C_n

The yawing moment Cn is positive for all values of side-slip angle β tested except one point in all of the three configurations.

The derivative of the yawing moment Cn with β, $Cn\beta$, is almost positive $Cn\beta > 0$ for all values of β tested in the Joined-wing (Fig.27) and the rear-wing configurations, while $Cn\beta \leqq 0$ for $\beta = 0° \sim 6°$ and $Cn\beta > 0$ for $\beta = 6° \sim 9°$ in the front-wing configuration.

In general, $Cn\beta > 0$ is required from the design standpoint for the airplane stability. The yawing moment of a Joined-wing is principally determined by the drag force difference between the right and left wings, and by the side force and its longitudinal station of action ; that is, the yawing moment becomes positive Cn>0 (nose to the right) by the swept-back angle of the front wing and by the side force acting on the vertical tail, while it becomes negative Cn<0 (nose to the left) by the swept-forward angle and the unhedral angle of the rear wing.

As for the present wind-tunnel model, the tail volume of the vertical tail is considered to be so small that the yawing moment Cn in the front-wing configuration, which should be sufficiently positive, remains very low level even if it is positive.

But, the $Cn\beta$ of the Joined-wing configuration is more positive than even the rear-wing configuration in spite of the above-mentioned adverse effect of the front-wing configuration which is actually pertinent to the present model. This is interpreted as an increase of the directional stability by the flow through the diamond-shaped duct formed by the front and rear wings.

IV. Conclusion.

Feasibility of making the Joined-wing concept fit for a practical application is discussed especially from the aerodynamics point of view not only theoretically by the extended-lifting-line theory, 3D-potential flow Panel method and a 3D-Euler finite difference computation but also experimentally by the low-speed wind-tunnel test.

To sum up the comparisons between possible geometric combinations of the front and rear wings, it is concluded ;

1) Three-dimensionally diamond-shaped Joined-wing configuration has higher value of lift-to-drag ratio than the planely joined-one.
2) The airplane efficiency is higher for the configuration with rear wing tip joined at partial spanwise station than at the tip of the front wing. The optimum spanwise location should, however, be determined not only from the aerodynamics but also from the structural dynamics and controls points of view.
3) The Joined-wing has more design freedom than the conventional ones, since the total lift force varies slightly with the change of area ratio and angles of sweep of the front and rear wings.

Taking these into account, the twist distributions were, then, designed for the swept-back front wing to have the wash-out distribution, and for the swept-forward rear wing to have the wash-in distribution and, in addition, to have positive incidence in average against the downwash effect from the front wing. The subsonic to transonic aerodynamic characteristics were obtained by a 3D-Euler finite difference computation. The drag-divergence Mach number proved to be higher than the design-point Mach number.

The lift characteristics obtained by the low-speed wind-tunnel test agreed well with the predictions by Panel method over the angle of attack range $0° \leqq \alpha \leqq 8°$. The test result reveals the dihedral effect $Cl\beta$ is undesirably positive in some range of small side-slip angle β. Further improvements on the location and tail volume of the vertical tail and more design effort on the dihedral and unhedral angles of the front and rear wings are required.

The major part of the present work was conducted as the cooperative research contract between Mitsui Engineering & Ship-Building Co.,Ltd. and National Aerospace Laboratory.

References

1. J.Wolkovitch : Joined Wing Research Airplane Feasibility Study, AIAA paper 84-2471
2. J.Wolkovitch : The Joined Wing : An Overview, J.Aircraft,Vol.23,No.3,March,1986, p.p.161
3. J.A.Clyde : Transonic Design and Wind-Tunnel Testing of a Joined-Wing Concept, AIAA paper 84-2433
4. M.F.Samuels : Structural Weight Comparison of a Joined-Wing and a Conventional Wing, J.Aircraft,Vol.19, No.6, June,1982, p.p.485
5. I.M.Kroo et al. : Aerodynamic and Structural Studies of Joined Wing Aircraft ; AIAA paper 87-2931
6. S.C.Smith et al.: The Design of a Joined-Wing Flight Demonstrator Aircraft , AIAA paper 87-2930
7. H.Fujieda et al.: Preliminary Wind-Tunnel Test of a Joined-Wing of Aft- and Forward-swept Wings, Proc.26th Aircraft Symp. (Oct.1988) JAPAN p.228
8. T.Fujita et al. : Low Speed Wind-tunnel Test on the Control Forces for Direct-Lift-and Side-Force-Controls of a Diamond- shaped Joined-Wing,Proc.27th Aircraft Symp.(Oct.1989) JAPAN p.498
9. H.Schlichting and E.Truckenbrodt : Aerodynamics of the Airplane,McGraw-Hill International Co.,1979.
10. L.Morino et al.: Steady Subsonic Flow around Finite Thickness Wings,NASA CR-2616 (1975)
11. M.Hashimoto et al.: Transonic Aerodynamics Analysis of Unconventional Wing Configurations by a 3D-Euler Code, Proc.ISCFD,Nagoya,Aug.1989
12. R.W.MacCormack et al.: The Effect of Viscosity in Hypervelocity Impact Cratering, AIAA paper 69-354
13. T.H.Pulliam et al.: Recent Improvements in Efficiency, Accuracy and Convergence for Implicit Approximate Factorization Algorithms, AIAA paper 85-0360
14. R.L.Bisplinghoff et al.: Aeroelasticity,Addison-Wesley, 1955

Table 1 Dimensions of the wind-tunnel test model

Length 1m	Span 0.84m	
	Front wing	Rear wing
Aspect ratio	8.0	4.76
Angle of sweep	30°	-30°
Taper ratio	0.313	0.313
dihedral / unhedral	10°	-25°
Span ratio	1	0.6

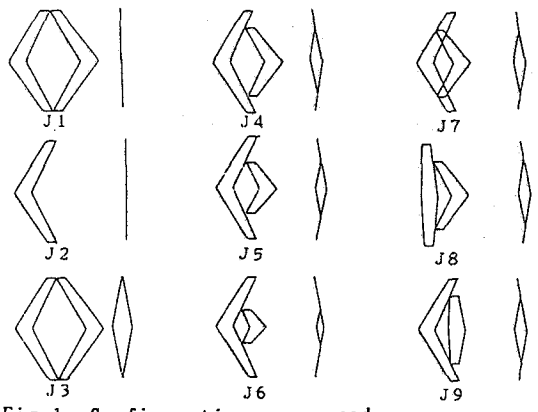

Fig.1 Configurations compared by the extended Lifting-Line theory

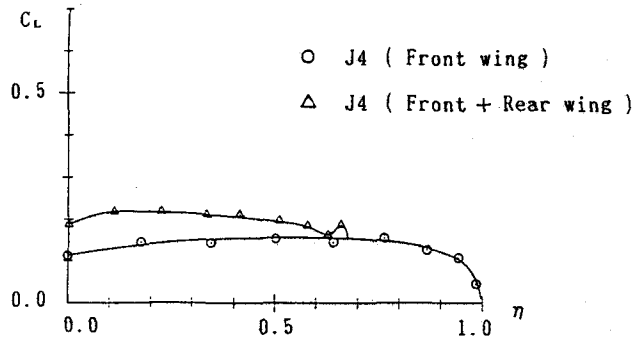

Fig.2 Spanwise lift distribution of J4 at $\alpha=2°$ by the extended Lifting-Line theory

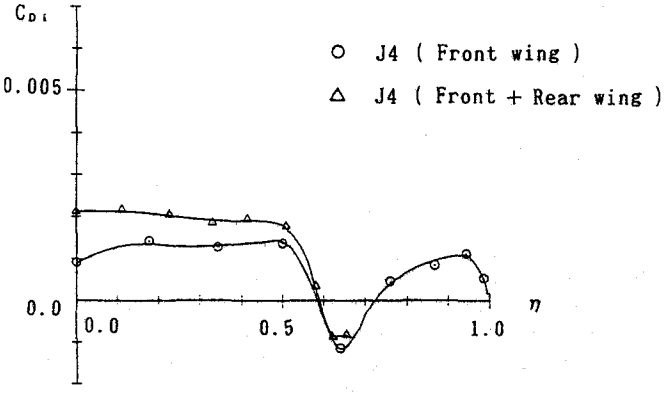

Fig.3 Spanwise distribution of induced-drag of J4 at $\alpha=2°$ by the extended Lifting-Line theory

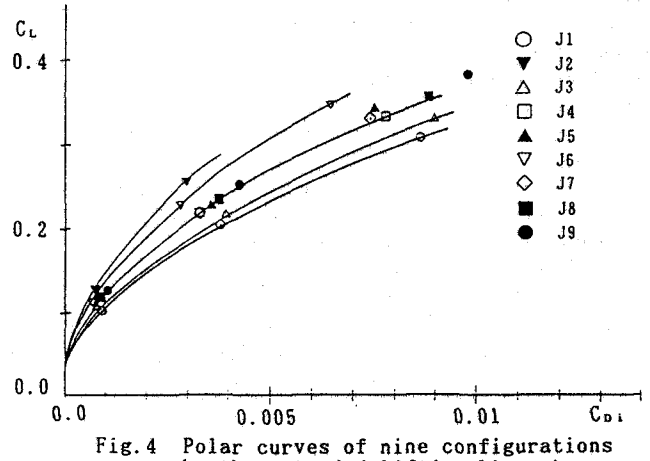

Fig.4 Polar curves of nine configurations by the extended Lifting-Line theory

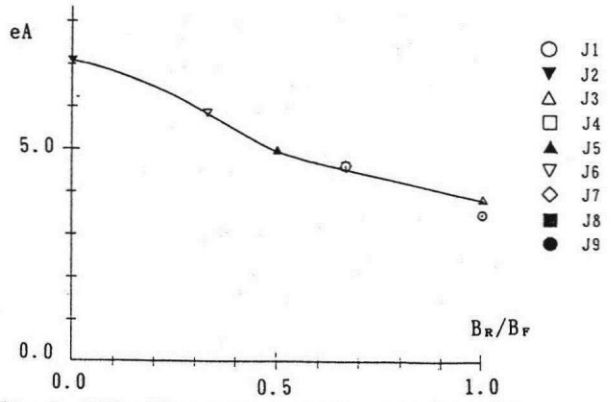

Fig.5 Effective aspect ratio as a function of span ratio B_R/B_F by the extended Lifting-Line theory

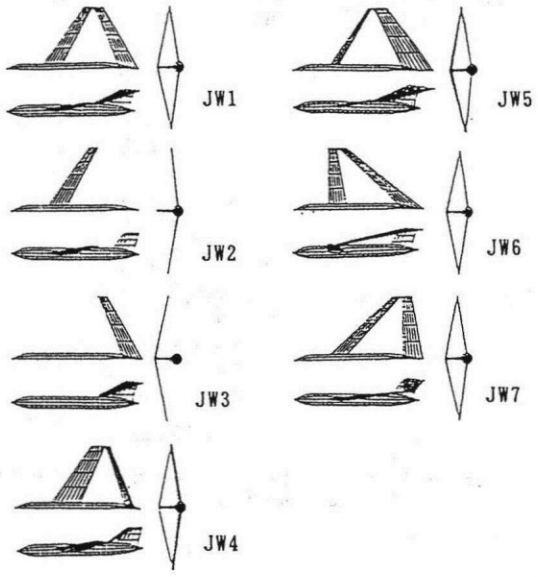

Fig.6 Configurations compared by the Panel methed

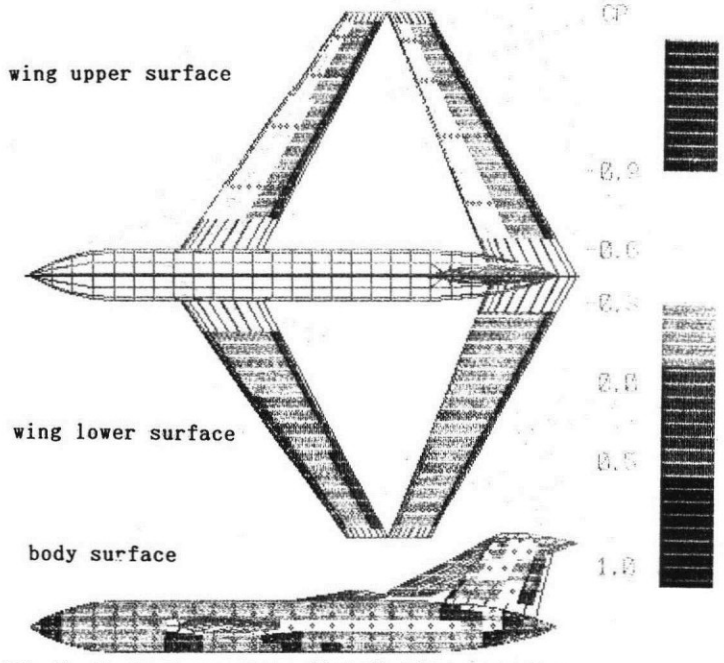

Fig.7 Typical pressure distribution over the Joined-wing configuration JW1 by the Panel method

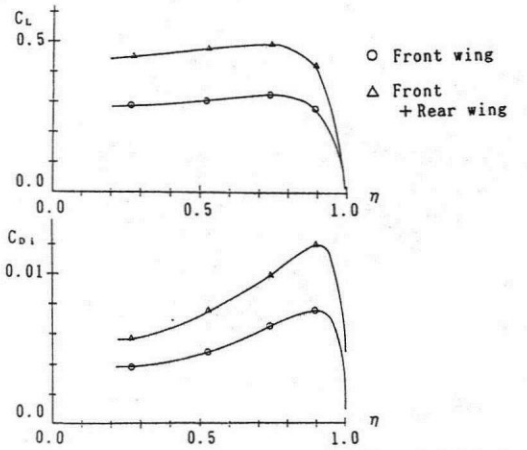

Fig.8 Spanwise distributions of lift and induced-drag of JW1 by the Panel method ($\alpha = 0°$)

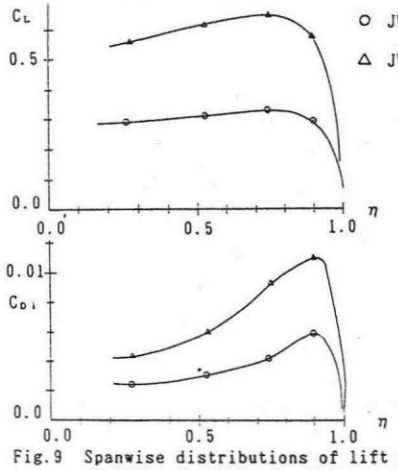

Fig.9 Spanwise distributions of lift and induced-dra of JW2 and JW3 by the Panel method ($\alpha = 0°$

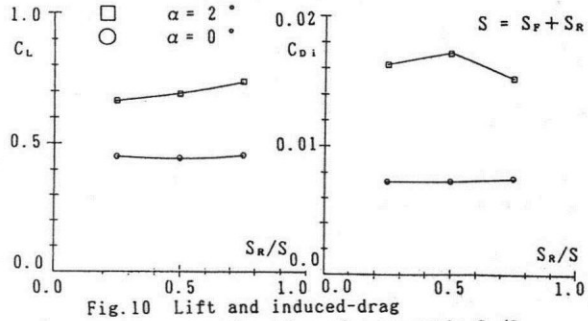

Fig.10 Lift and induced-drag as a function of area ratio S_R/S

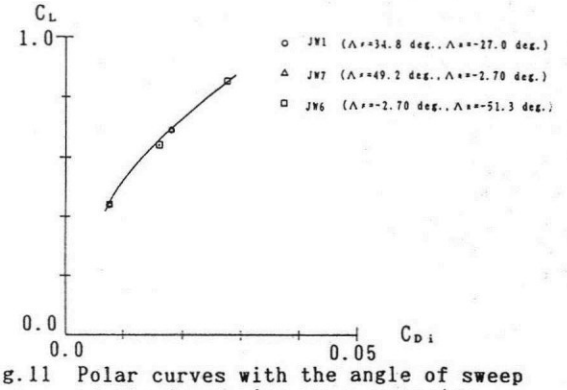

Fig.11 Polar curves with the angle of sweep of the front wing as a parameter

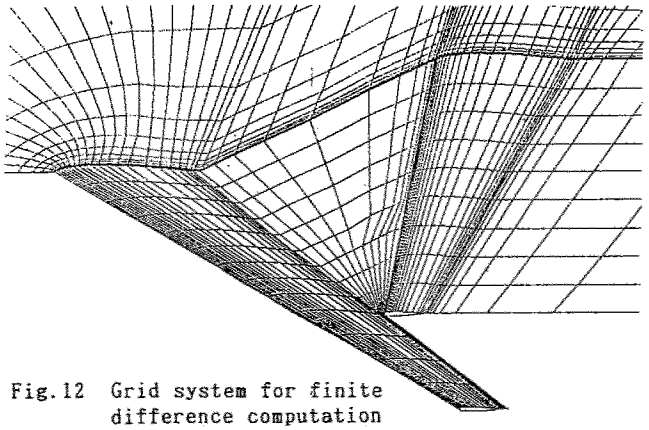

Fig.12 Grid system for finite difference computation

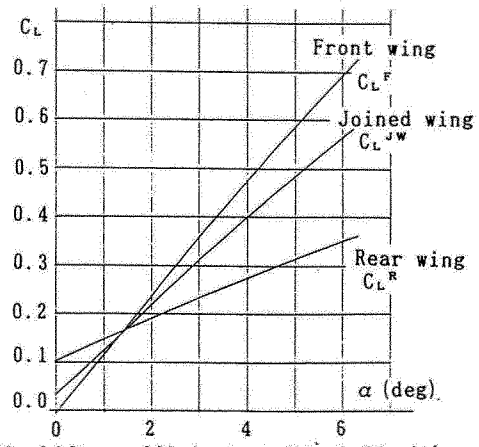

Fig.13 Lift coefficient at M∞=0.75 with α varied (CFD result by Euler eq)

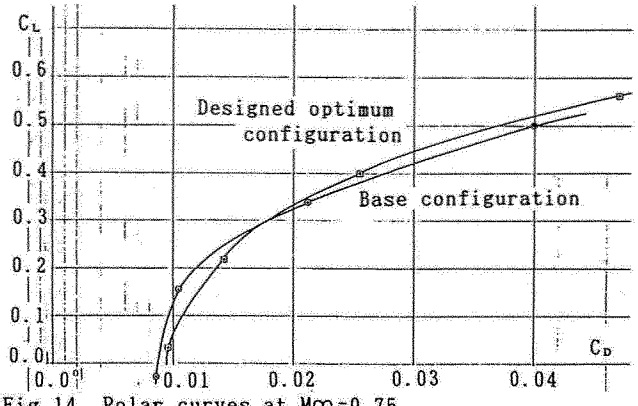

Fig.14 Polar curves at M∞=0.75 (CFD result by Euler eq)

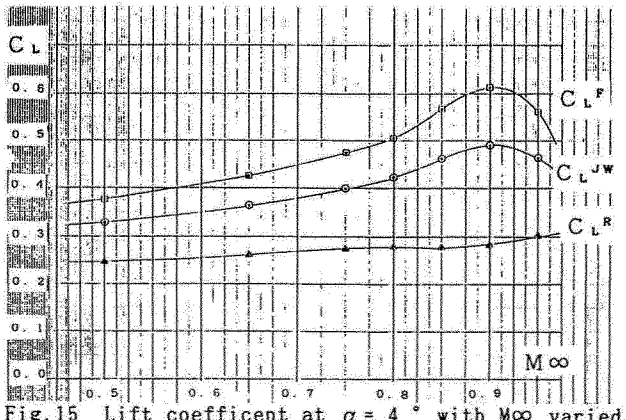

Fig.15 Lift coefficent at α = 4 ° with M∞ varied (CFD result by Euler eq)

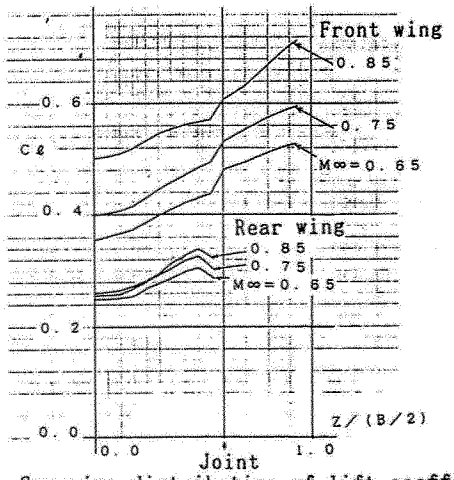

Fig.16 Spanwise distribution of lift coefficient at α = 4 ° (CFD result by Euler eq)

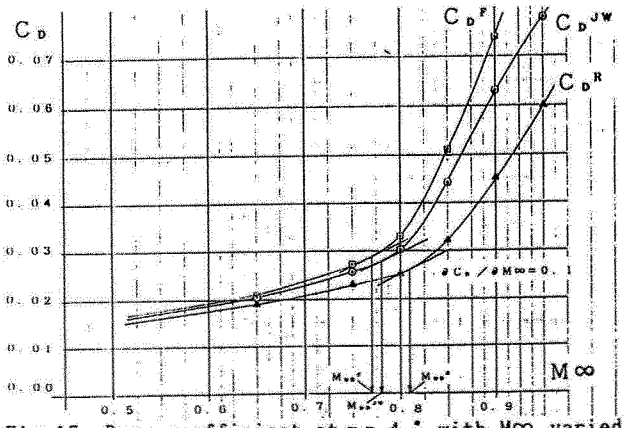

Fig.17 Drag coefficient at α = 4 ° with M∞ varied (CFD result by Euler eq)

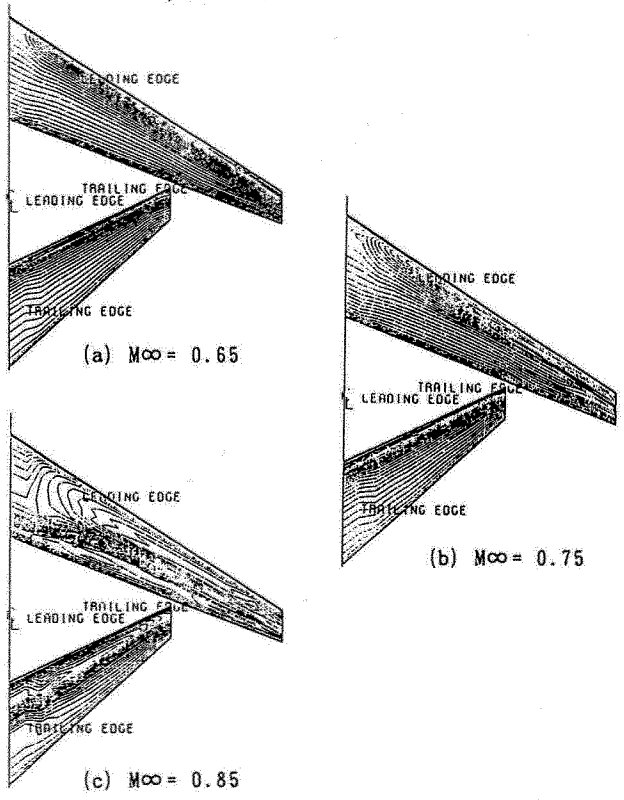

Fig.18 Cp-contours over wing surfaces at α = 4 °

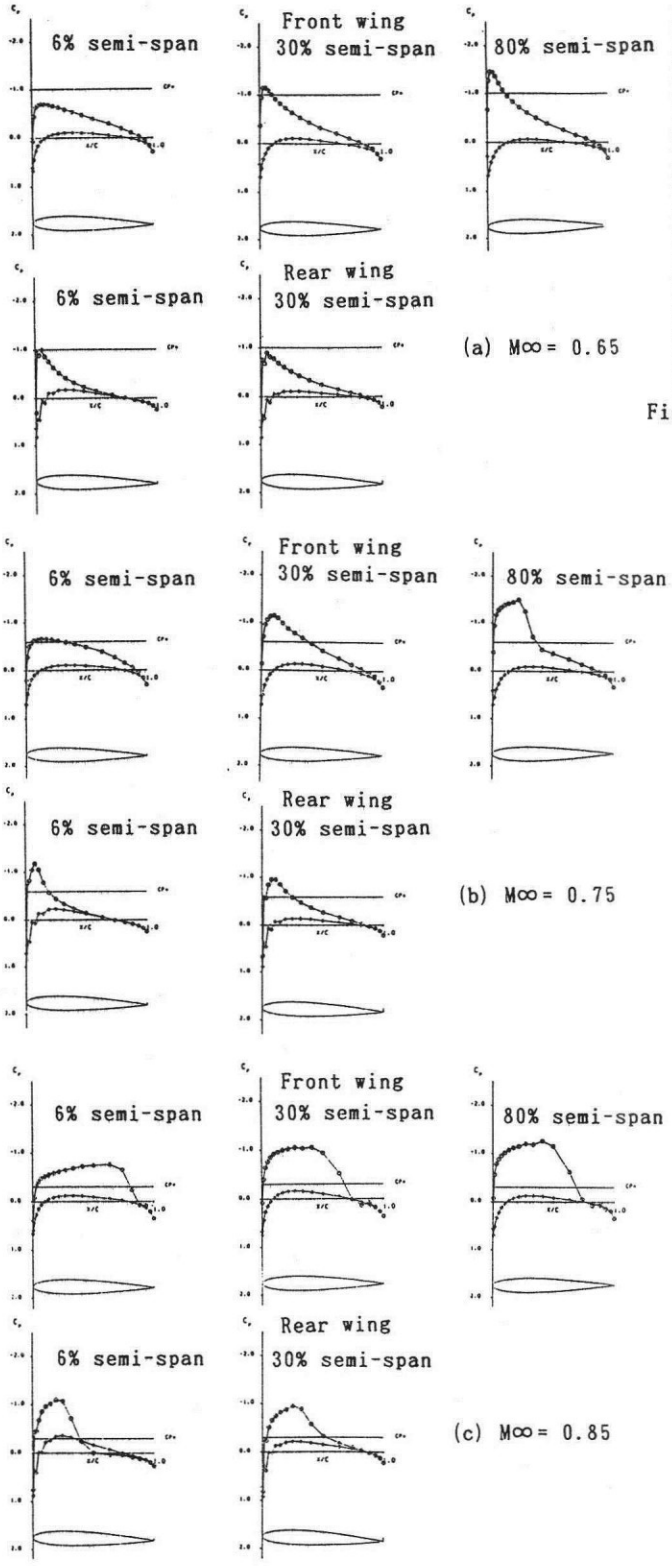

Fig.19 Chordwise pressure distributions at $\alpha = 4°$

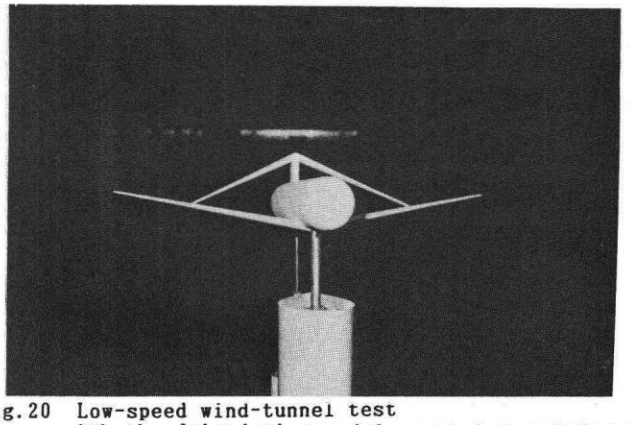

Fig.20 Low-speed wind-tunnel test with the Joined-wing model mounted on a balance

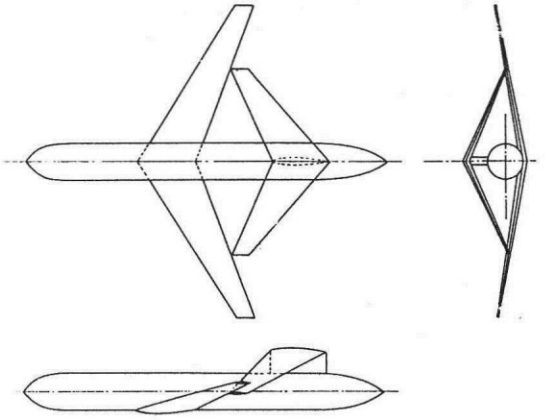

Fig.21 Wind-tunnel test model

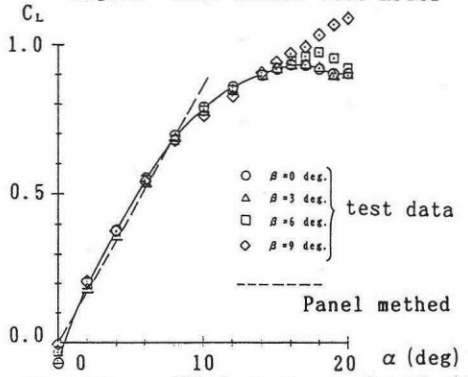

Fig.22 Lift coefficient vs. angle of attack (Wind-tunnel test data)

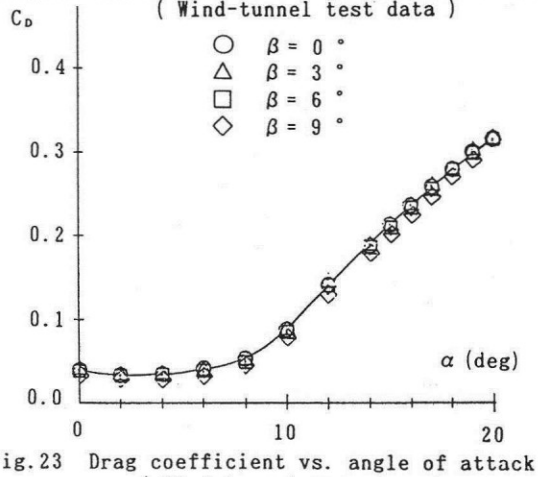

Fig.23 Drag coefficient vs. angle of attack (Wind-tunnel test data)

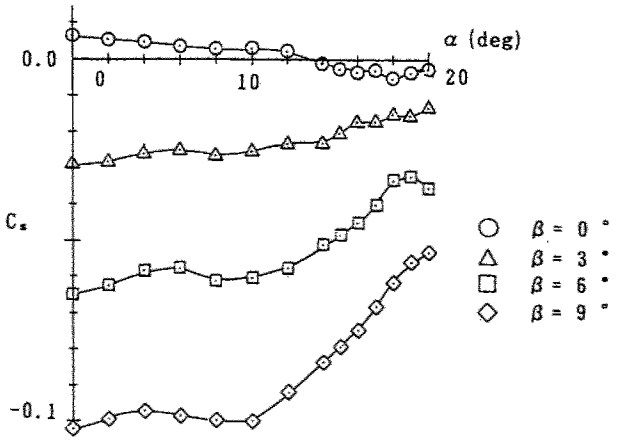

Fig.24 Side-force coefficient vs. angle of attack
(Wind-tunnel test data)

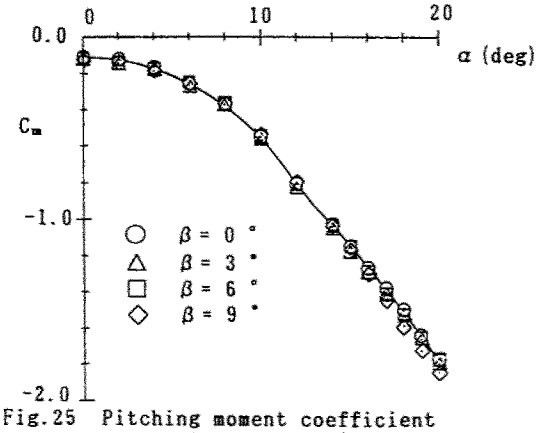

Fig.25 Pitching moment coefficient
vs. angle of attack(Wind-tunnel test data)

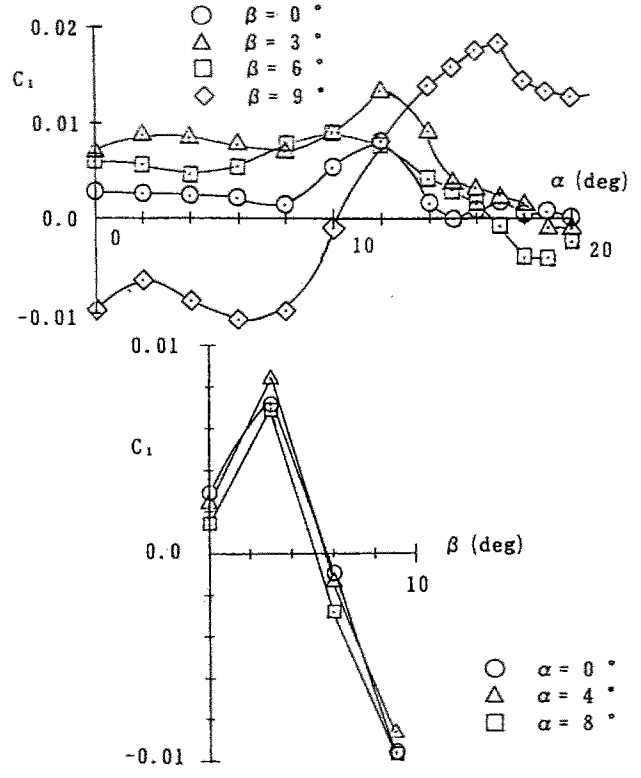

Fig.26 Rolling moment coefficient
(Wind-tunnel test data)

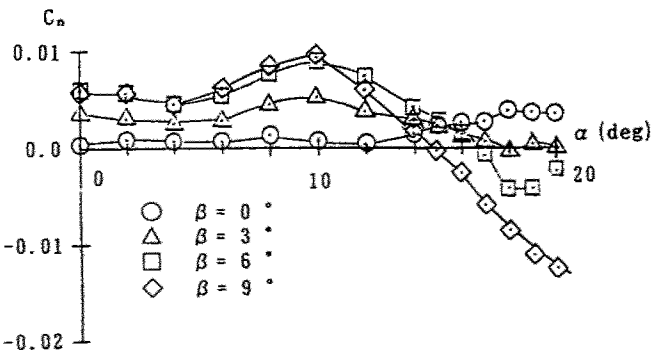

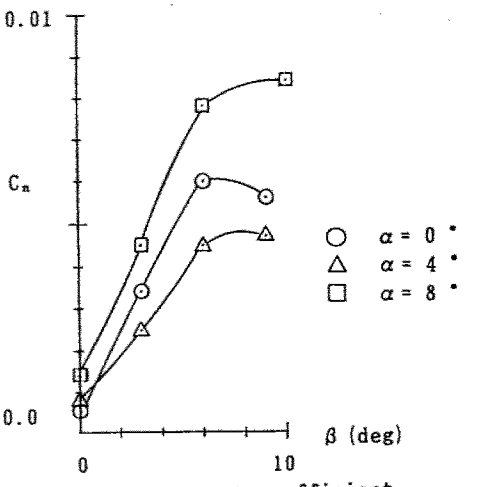

Fig.27 Yawing moment coefficient
(Wind-tunnel test data)